Laser-ultrasonic monitoring of ferrite recovery in ultra low carbon steel
Smith, A.; Krüger, S. E.; Sietsma, J.; van der Zwaag, S.

National Research Council Canada   Conseil national de recherches Canada

Canada

Laser-ultrasonic monitoring of ferrite recovery in ultra low carbon steel

A. Smith [a,b,*], S.E. Kruger [c], J. Sietsma [b], S. van der Zwaag [d]

[a] *Netherlands Institute for Metals Research, 2628 AL Delft, The Netherlands*
[b] *Department of Materials Science and Engineering, Delft University of Technology, 2628 AL Delft, The Netherlands*
[c] *IMI-National Research Council of Canada, 75 Boul. de Mortagne, Boucherville, Quebec, Canada J4B 6Y4*
[d] *Faculty of Aerospace Engineering, Delft University of Technology, 2629 HS Delft, The Netherlands*

Abstract

The static recovery kinetics of warm deformed ferrite have been characterized by a combination of in situ laser ultrasonics and stress relaxation measurements. During recovery the ultrasonic velocity change decreased whilst the ultrasonic attenuation generally remained constant. The velocity change was explained in terms of dislocation damping, whilst for the attenuation the results were due to a combination of grain scattering and dislocation damping. From the ultrasonic velocity and attenuation measurements, the dislocation density and pinning point separation have been determined using a model in the literature. These values have been compared to those obtained from stress relaxation data for the same experimental conditions. The results showed that the difference in calculated dislocation densities differed by one or two orders of magnitude. The difference in the values of pinning point separation was about one order of magnitude. Finally possible reasons for these differences have been discussed with reference to the dislocation structure present during recovery.
© 2007 Elsevier B.V. All rights reserved.

Keywords: Ultrasonic; Stress relaxation; Recovery; Dislocation density; Ultra low carbon steel

1. Introduction

Laser ultrasonics is a relatively recent technique that uses laser light pulses to generate and detect ultrasonic waves in materials. Due to the interaction of the microstructure with the ultrasonic waves, various phenomena can be studied. The literature on ultrasonics has mostly focused on: grain size measurement [1–3], monitoring of phase transformations [4,5], recrystallization [3,6–8], magnetic domain effects [9,10] and dislocation behaviour [10–14].

A key advantage of this technique is that it is non-contact and non-destructive. Thus, it has great potential to be used in industrial online monitoring of microstructural development during materials processing. Indeed trials have already been performed during the processing of steel strip [15], sheet [16] and a system has been continuously operating for a few years for monitoring tube thickness and austenite grain size [17].

Whilst some progress has been made, there is a lack of ultrasonic studies of annealing behaviour following warm or hot deformation of steels. The studies mentioned earlier concerning recrystallization were performed on samples annealed after cold deformation only. Similarly, the ultrasonic studies concerning dislocation behaviour were mainly focused on creep [11], ageing [12] and fatigue [13,14]. Thus, if ultrasonics is to be used for online monitoring of recovery and recrystallization after hot forming in steels, then further study is required.

Currently these two phenomena are best studied by using the more established in situ stress relaxation technique [18–21]. It can be argued that a combination of stress relaxation measurements and simultaneous ultrasonic measurements will strongly facilitate the interpretation of ultrasonics data. This concept will be applied in the present paper.

This investigation focuses on the recovery process in ferrite following warm deformation. An ultra low carbon (ULC) steel was chosen for this investigation, since it is known (and confirmed here) that recrystallization following warm deformation is unlikely to occur, except for longer annealing times [22–24].

In the current investigation, measurements of ultrasonic velocity and attenuation have been made during annealing for a variety of deformation conditions and at various

* Corresponding author at: Netherlands Institute for Metals Research, 2628 AL Delft, The Netherlands. Tel.: +39 65055461.
E-mail address: alismith.mec@c-s-m.it (A. Smith).

temperatures. Stress relaxation measurements were made simultaneously.

In addition samples were quenched after various annealing times and analysed by optical microscopy.

2. Effect of microstructure on ultrasonic velocity and attenuation

Microstructural features cause changes in ultrasonic velocity and attenuation. The ultrasonic velocity mainly depends on texture [6,7], the dislocation structure [13,14], magnetomechanical effects [25] and on scattering effects. Scattering is caused by acoustic inhomogeneities, like grains, porosity, cracks, etc. Given the perfection of the steel samples used, in this study only grain scattering needs to be considered.

The attenuation of ultrasonic waves is due to grain scattering and absorption effects. Absorption is mainly due to the dislocation structure [11–14] and magnetomechanical effects [9,10].

Thus, the ultrasonic velocity and attenuation during annealing should be due to a combination of some or all of the above effects, depending on the deformation and temperature conditions. In the following sections the theory for each of these effects is discussed.

2.1. Dislocation damping

The effect of dislocations on velocity and attenuation has been treated by Granato and Lucke [26]. In their model, a dislocation is regarded as a string that vibrates between pinning points. Forced vibration of the dislocation occurs by the interaction of the dislocation with the ultrasonic waves. In addition, the motion of the dislocation is inhibited by a drag force. The magnitude of this depends on a combination of thermal vibrations (phonons), electrons, and impurity atoms.

Assuming strain amplitude independent damping, the velocity change $(v_d(\rho) - v_d(0)/v_d(0))$ and attenuation α_d (in dB/s) due to the presence of dislocations with density ρ and average pinning point separation L, are given by equations [26]:

$$\left(\frac{v_d(\rho) - v_d(0)}{v_d(0)}\right) = \left(\frac{4Gb^2\rho L^2}{\pi^4 C}\right)\left(\frac{1-\beta^2}{(1-\beta^2)^2 + (\beta^2/g^2)}\right) \tag{1}$$

$$\alpha_d = \frac{4fGB\rho L^2}{0.115\pi^5 Cf_{0d}\Lambda}\left(\frac{\beta}{(1-\beta^2)^2 + (\beta^2/g^2)}\right) \tag{2}$$

where $v_d(\rho)$ is the velocity due to dislocations, $v_d(0)$ the velocity when there are no dislocations, G the shear modulus, b the Burgers vector, C the dislocation line tension, B the damping constant, f the frequency of the ultrasonic waves, f_{0d} the resonance frequency of the dislocations and Λ is the density of the material. The factors β and g are given by

$$\beta = \frac{f}{f_{0d}} \tag{3}$$

$$g = \frac{2\pi^2\Lambda b^2 f_{0d}}{B} \tag{4}$$

A maximum in attenuation occurs at the resonance frequency, given by

$$f_{0d}^2 = \frac{C}{4\pi\Lambda b^2 L^2} \tag{5}$$

When β and β^2/g^2 are small, then Eqs. (1) and (2) can be approximated by

$$\left(\frac{v_d(\rho) - v_d(0)}{v_d(0)}\right) = \left(\frac{4Gb^2\rho L^2}{\pi^4 C}\right) \tag{6}$$

$$\alpha_d = \frac{16GBb^2 f^2\rho L^4}{0.115\pi^4 C^2} \tag{7}$$

As can be seen from Eqs. (1)–(5), for isothermal annealing, the velocity change and attenuation are dependent on the dislocation density and pinning point separation only.

2.2. Magnetomechanical damping

The interaction of magnetic domain walls with ultrasonic waves gives rise to magnetomechanical damping. In the absence of an applied magnetic field two effects dominate: micro-eddy current damping and hysteresis damping. For ultrasonic waves in the MHz range (used in this study), the first effect dominates [27].

In the micro-eddy current mechanism, ultrasonic waves cause the movement of magnetic domain walls. This leads to changes in local magnetization, giving rise to micro-eddy currents [28]. This contribution depends on the ultrasonic frequency but not on its amplitude [29].

The velocity change $(v_{me}(\mu_i) - v_{me}(0)/v_{me}(0))$ and attenuation α_{me} in this case are given by [30]:

$$\left(\frac{v_{me}(\mu_i) - v_{me}(0)}{v_{me}(0)}\right) = \left(\frac{0.225}{1 + f^2/f_{0r}^2}\right)\left(\frac{\mu_i\lambda_s^2 E_{sat}}{I_s^2}\right) \tag{8}$$

$$\alpha_{me} = \left(\frac{0.45f}{0.115}\right)\left(\frac{\mu_i\lambda_s^2 E_{sat}}{I_s^2}\right)\left(\frac{f/f_{0r}}{1 + f^2/f_{0r}^2}\right) \tag{9}$$

where $v_{me}(\mu_i)$ is the velocity in the presence of magnetic domains and $v_{me}(0)$ the velocity when there are no domains, μ_i the initial permeability, λ_s the magnetostriction constant, E_{sat} the Young's modulus at saturation, I_s the saturation magnetisation and f_{0r} is the relaxation frequency given by the following equation:

$$f_{0r} = \frac{\pi R_e}{24\mu_i D_d^2} \tag{10}$$

where R_e is the electrical resistivity and D_d is the domain size.

The initial permeability in Eqs. (8) and (9) also depends on the internal stress σ_i. According to Becker and Kersten, the initial permeability as quoted by Degauque [28], is given by

$$\mu_i = \frac{8\pi I_s^2}{9\lambda_s\sigma_i} \tag{11}$$

Thus it can be seen, in micro-eddy current damping, the presence of internal stresses will act to reduce the velocity change and attenuation.

2.3. Texture effects

In the presence of texture, the longitudinal ultrasonic velocity v_{Lx} is given by [6]:

$$v_{Lx} = \sqrt{\left(\frac{1}{\Lambda}\left((\lambda + 2\mu) + \left(\frac{32\sqrt{2}}{35}\pi^2 c W_{400}\right)\right)\right)} \quad (12)$$

where Λ is the density of the material, λ, μ and c are single crystal elastic constants and W_{400} is a texture coefficient. This coefficient comes from a series expansion of the crystallographic orientation distribution function. For an orthorhombic aggregate of cubic crystallites W_{400} is one of the lowest order non-zero texture coefficients in the Roe notation [6,16].

During isothermal conditions the elastic constants and density can be assumed constant. In addition in most metals the texture term $(32\sqrt{2}/35)\pi^2 c W_{400}$ is much smaller than the constant term $(\lambda + 2\mu)$, thus Eq. (12) can be simplified to:

$$v_{Lx} = d + e W_{400} \quad (13)$$

where d and e are the constants. Thus, from Eq. (13) the velocity is linearly related to the texture coefficient.

2.4. Grain scattering effects

Grain scattering affects both the velocity and attenuation of ultrasonic waves. The relationships between velocity and grain size or attenuation and grain size depend on the ratio of the ultrasonic wavelength in the material λ_u to the grain size D_g. For the experimental results presented here, the ultrasonic wavelength in the material is around an order of magnitude larger than the average deformed grain size. Thus, assuming the Rayleigh regime ($\lambda_u \gg D_g$), the group velocity v_{LGg} and attenuation α_{Lg} for longitudinal waves are given by [31,4]:

$$v_{LGg} = \frac{v_L}{1 + (A/\Lambda v_L^2)^2 (2/(3 \times 5^3 \times 7))(14 + (21\kappa^2/k^2) + (6/5)(106/7)(6\kappa^2/7k^2)(21\kappa^4/k^4)(kD_g)^2)} \quad (14)$$

$$\alpha_{Lg} = S_L D_g^3 f^4 \quad (15)$$

where A is a single-crystal anisotropy factor and S_L is the scattering factor in the longitudinal direction.

The wave numbers κ and k in Eq. (14) are given by [31]:

$$\kappa = \frac{2\pi f}{v_s} \quad (16)$$

$$k = \frac{2\pi f}{v_L} \quad (17)$$

where v_s is the shear wave velocity.

For Eq. (15), the scattering factor for longitudinal waves S_L, is given by [32]:

$$S_L = \frac{0.0308\pi^4 \mu_a^2}{\Lambda^2 v_L^2}\left(\frac{2}{v_L^5} + \frac{3}{v_s^5}\right) \quad (18)$$

where μ_a is related to the anisotropy of the grain, and is defined as

$$\mu_a = c_{11} - c_{12} - 2c_{44} \quad (19)$$

where c_{11}, c_{12} and c_{44} are the elastic constants of the cubic crystal.

It should be noted that in the above equations the grains are assumed to be spherical. Thus, for the majority of results in this study, where a deformation strain of 0.15 was used, Eqs. (14) and (15) should give reasonable estimates of the grain scattering effect.

2.5. Total effect of microstructure

To summarise, the overall velocity change $(\Delta v/v_0)_T$ and attenuation α_T due to microstructure, can be expressed as

$$\left(\frac{\Delta v}{v_0}\right)_T = \left(\frac{v_{Lx}(W_{400}) - v_{Lx}(0)}{v_{Lx}(0)}\right)$$
$$+ \left(\frac{v_{LGg}(D_g) - v_{LGg}(\infty)}{v_{LGg}(\infty)}\right) + \left(\frac{v_d(\rho) - v_d(0)}{v_d(0)}\right)$$
$$+ \left(\frac{v_{me}(\mu_i) - v_{me}(0)}{v_{me}(0)}\right) \quad (20)$$

$$\alpha_T = \alpha_d + \alpha_{me} + \alpha_g \quad (21)$$

where $v_{Lx}(0)$ and $v_{LGg}(\infty)$ are the velocities in the absence of texture ($W_{400} = 0$, Eq. (12)) and grain scattering ($D_g = \infty$, Eq. (14)), respectively. In obtaining v_0 the minimum values observed in the time scale of each experiment were used.

In the case of recovery in ferrite following plastic deformation, the grain size should be constant (i.e. constant $((v_{LGg}(D_g) - v_{LGg}(\infty))/v_{LGg}(\infty))$) and there should be a constant texture (i.e. constant $((v_{Lx}(W_{400}) - v_{Lx}(0))/v_{Lx}(0))$). This means that as recovery proceeds, any change in $(\Delta v/v_0)_T$ will be due only to dislocation damping and magnetomechanical damping.

Using Eq. (15) the grain size effect can be subtracted from experimental measurements of attenuation therefore:

$$\alpha_T = \alpha_d + \alpha_{me} \quad (22)$$

Furthermore, from Eqs. (8)–(11) the magnetomechanical damping is expected to be small during the initial stages of recovery (large internal stress) and should increase as recovery proceeds.

3. Experimental

The composition of the ULC steel used in the experiments is shown in Table 1.

Table 1
Steel composition shown in wt%

C	0.0024
Mn	0.561
Si	0.147
Al	0.038
Fe	Balance

Cylindrical samples were machined from rolled plate, with diameter 10 mm and length 12 mm. The samples were machined with the axis parallel to the rolling direction.

Fig. 1A shows the experimental set-up used for the ultrasonic measurements. A Nd:YAG laser (pulse energy of 200 mJ, pulse duration of 5 ns, wavelength of 532 nm) is used to generate ultrasonic waves in the deformed sample. The ultrasonic waves propagate through the sample and are reflected off the back surface. Each time the waves reach the original sample surface a small displacement of the surface occurs. These "echoes" are detected by a second laser (pulse duration of 50 μs, peak power of 1 kW, wavelength of 1064 nm) coupled to an confocal Fabry–Perot interferometer. The signals are digitised and recorded for further processing. Fig. 1B shows an example of a signal obtained after deformation. The signals are used to calculate the ultrasonic velocity and attenuation. The velocity was determined by the ratio of the distance travelled through the material (twice the sample diameter) to the time delay between generation and the first echo. The attenuation (determined for a range of frequencies) was obtained from the ratio of the amplitude of the first echo to the second echo. This allowed an attenuation versus frequency curve to be obtained for each measurement. Finally, this curve should be corrected for diffraction effects to provide the true attenuation of the material. However, due to the sample geometry present after deforma-

tion (barreled cylinder), a diffraction correction could not be made.

To investigate the relaxation kinetics after plastic deformation, a Gleeble® 3500 thermo-mechanical simulator coupled with a laser ultrasonic monitoring device was used. Each test comprised of three stages. Firstly the desired starting microstructure was made via austenitisation at 1100 °C for 3 min under vacuum. Then, the samples were cooled to the desired test temperature in the ferritic state. Secondly, after holding for 5 min, the samples were deformed in compression. Lubrication was provided via graphite paste. To protect the steel against the possibility of carbon pick-up during the test, tantalum sheets were used as a protective layer between the sample and the lubricant. Just before deformation the Gleeble® chamber was filled with argon, since this provided better conditions for the generation of ultrasonic waves.

Finally in the third stage, the annealing kinetics after deformation were monitored via both the stress relaxation and laser ultrasonics techniques. In the stress relaxation technique the stress required to maintain a constant strain in the sample is recorded. In the laser-ultrasonics technique the ultrasonic signals were recorded for later calculation of velocity and attenuation.

To investigate the microstructural development during annealing, selected samples were water quenched after different annealing times in the third stage. To provide less interference with the ultrasonic measurements, the quenching was carried out using a separate Gleeble® 3500 for the same experimental conditions. Samples were quenched with a rate of approximately 200 °C/s. The samples were then analysed by optical microscopy after suitable metallographic preparation.

4. Results

4.1. Microstructural evolution

Figs. 2–4 show examples of the microstructural changes during annealing.

As can be seen from Fig. 2, after 3000 s annealing at 550 °C for a strain of 0.5, the microstructure consists
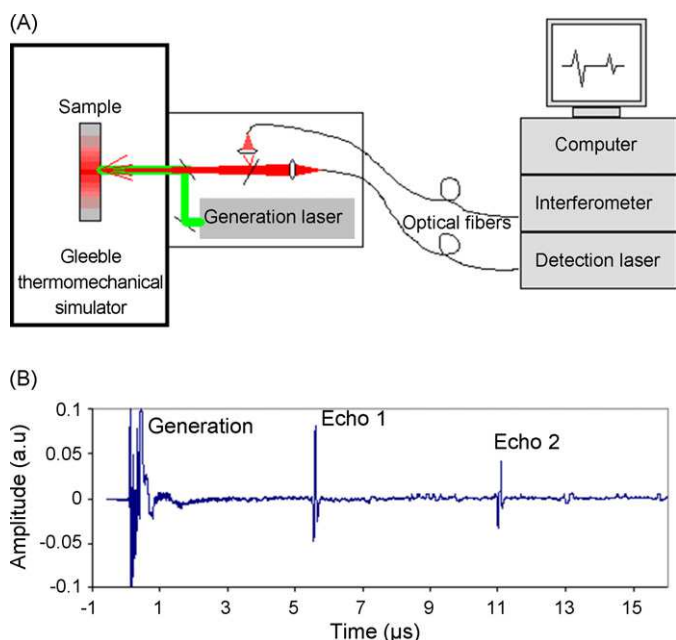

Fig. 1. (A) Laser ultrasonic monitoring apparatus. (B) Example of signal obtained.

Fig. 2. Optical micrograph of ULC steel after 3000 s annealing. Deformation and annealing temperature = 550 °C, strain = 0.5, strain rate = 0.1 s^{-1}.
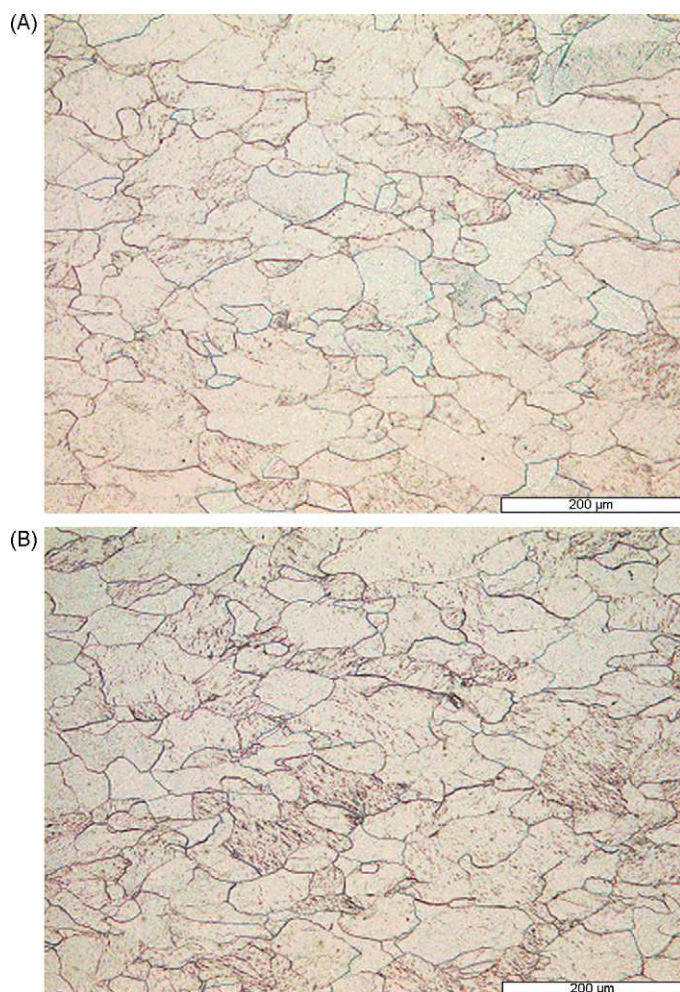
(A)

(B)

Fig. 3. Optical micrographs after annealing at 730 °C. Strain = 0.15, strain rate = 0.1 s^{-1}. (A) 36 s; (B) 200 s.

(A)

(B)

Fig. 4. Optical micrographs after annealing at 800 °C. Strain = 0.15, strain rate = 0.1 s^{-1}. (A) 14 s; (B) 300 s.

of a deformed grain structure with no sign of recrystallization.

After 36 s annealing at 730 °C for a strain of 0.15, Fig. 3A shows a deformed grain structure. Some grains however seem to have a clean interior and have negative curvature. After 200 s (Fig. 3B), the structure appears similar. Thus, it is difficult to decide whether or not recrystallization has begun.

After 14 s annealing at 800 °C for a strain of 0.15, Fig. 4A shows a deformed structure with some grains possessing a clean interior. After 300 s (Fig. 4B), the structure appears partially recrystallized with very large grains.

In light of the uncertainty in determining the transition between pure recovery and the start of recrystallization, only the first 10 s of annealing will be considered in the following results and discussion for $T = 730$ and 800 °C. This is highlighted by the dotted lines in Fig. 5. For $T = 550$ °C the whole time range is considered.

4.2. Effect of temperature

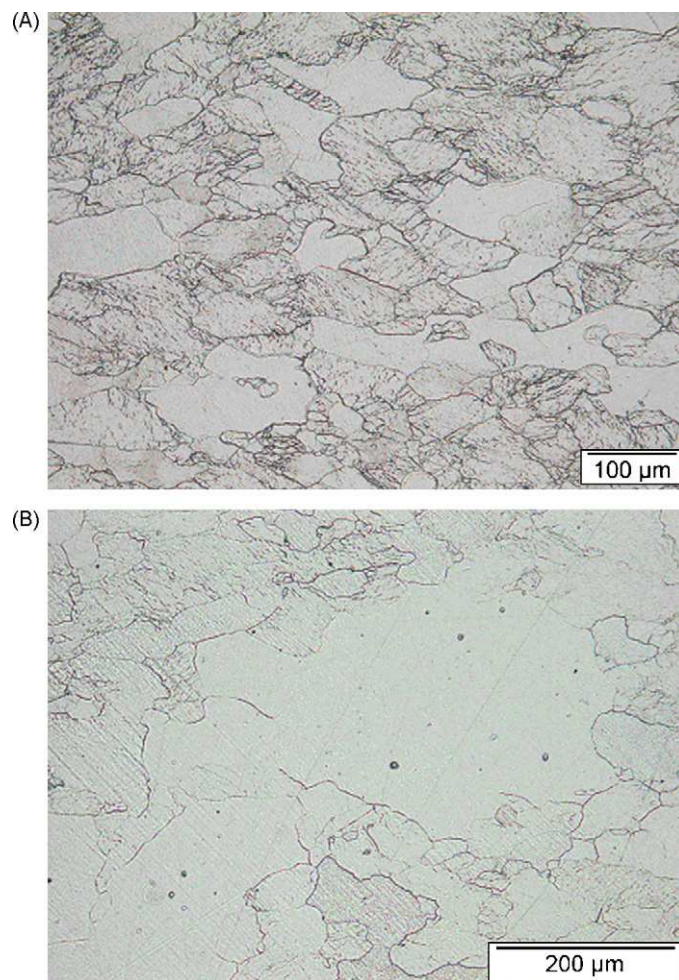Fig. 5 shows the effect of temperature on stress relaxation, ultrasonic velocity and attenuation. It should be noted that in all figures concerning ultrasonic velocity, the fractional change in velocity ($\Delta v/v_0$) is plotted. In each experiment v_0 was taken to be the value at 100 s annealing. In addition for the attenuation, only the results for a frequency of 8 MHz are shown. Similar trends were found for other frequencies. However, for lower frequencies changes in attenuation are less clear, whilst for higher frequencies the experimental scatter becomes much larger. Thus, it was found that the data collected at 8 MHz, offered the best compromise between the above-mentioned effects.

As can be seen from Fig. 5A the stress decreases with time for all annealing temperatures. Also it can be seen that the initial stress decreases with increasing temperature. This is due to faster dynamic recovery occurring as at higher temperatures. In addition, the rate of stress relaxation appears to decrease between 550 and 800 °C.

Analysis of the fractional ultrasonic velocity change in Fig. 5B yields similar trends. The initial values decrease with increasing temperature (although for 730 and 800 °C the values are similar) and the rate of change in ($\Delta v/v_0$) with time appears to decrease slightly from 550 to 800 °C.

From Fig. 5C, the ultrasonic attenuation appears generally larger for a higher temperature. In addition, the attenuation at
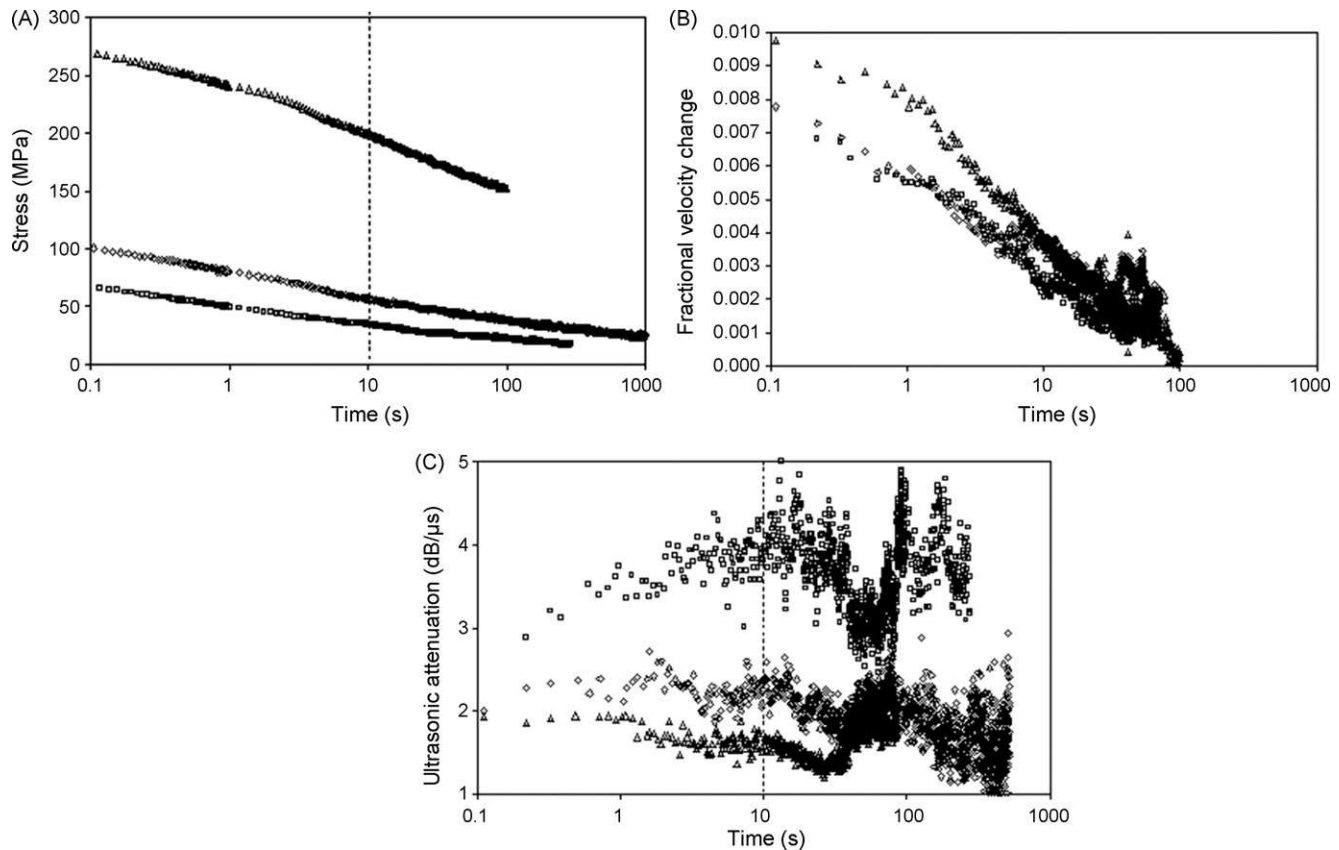
Fig. 5. (A) Stress, (B) fractional ultrasonic velocity change and (C) attenuation for strain = 0.15 and strain rate = 0.1 s^{-1}. Open triangles = 550 °C, open diamonds = 730 °C and open squares = 800 °C. Attenuation results are for an ultrasonic frequency of 8 MHz.

550 and 730 °C appears constant, whilst at 800 °C it tends to increase.

4.3. Effect of applied strain

Fig. 6 shows the effect of strain on stress relaxation, ultrasonic velocity and attenuation.

The stress relaxation data in Fig. 6A indicate that a higher strain gives rise to a higher initial stress and that both curves are almost parallel, indicating similar rates of softening.

Analysis of the fractional ultrasonic velocity change in Fig. 6B shows that for the higher strain the initial value after deformation is higher. In addition, the rate of change in $(\Delta v/v_0)$ with time appears similar for both strains.

From Fig. 6C, it can be seen that the ultrasonic attenuation is higher for the lower applied strain. In addition, for both strains the attenuation remains approximately constant during annealing, although some fluctuations are observed.

5. Discussion

As explained earlier, for a constant grain size and texture the values of $\Delta v/v_0$ should only change with time due to changes in dislocation damping and magnetomechanical damping. For the attenuation the values of α_T should also depend on the above effects with the addition of a grain scattering effect, since not the change in α_T, but the absolute value is considered.

The contribution of magnetomechanical damping to the observed velocity changes and attenuation can be assessed with reference to Fig. 5B and C and the Curie temperature. For the steel used in this investigation the Curie temperature is around 768 °C [10]. Hence, differences in the data for $T = 550$ °C (ferromagnetic behaviour) and $T = 800$ °C (paramagnetic behaviour) may reveal the magnitude of the effect.

From Fig. 5B there is a decrease in the velocity change between 550 and 800 °C suggesting the loss of the magnetomechanical effect described by Eq. (8). However, with reference to Fig. 5A, at 550 °C there is a much higher stress (dislocation density) compared to that at 800 °C. Thus, it is also likely that the decrease in the velocity change is due to a decrease in dislocation damping, i.e. in ρL^2 from Eq. (6). An indication of the dominating effect can be obtained with reference to Eqs. (11) and (8), where it can be seen that larger internal stresses (due to dislocations) should give rise to a smaller magnetomechanical damping effect. Thus, it is suggested that the experimental velocity change values are mostly due to dislocation damping.

From the attenuation results it can be seen in Fig. 5C that the values at 800 °C are significantly higher than at 550 °C. There is no drop in attenuation at 800 °C, which would be expected from Eq. (9) if there was significant magnetomechanical damping. Assuming a constant grain size, the trend of increasing attenuation with increasing temperature in Fig. 5C should be therefore mostly due to a change in dislocation damping, i.e. an increase in ρL^4 from Eq. (7).
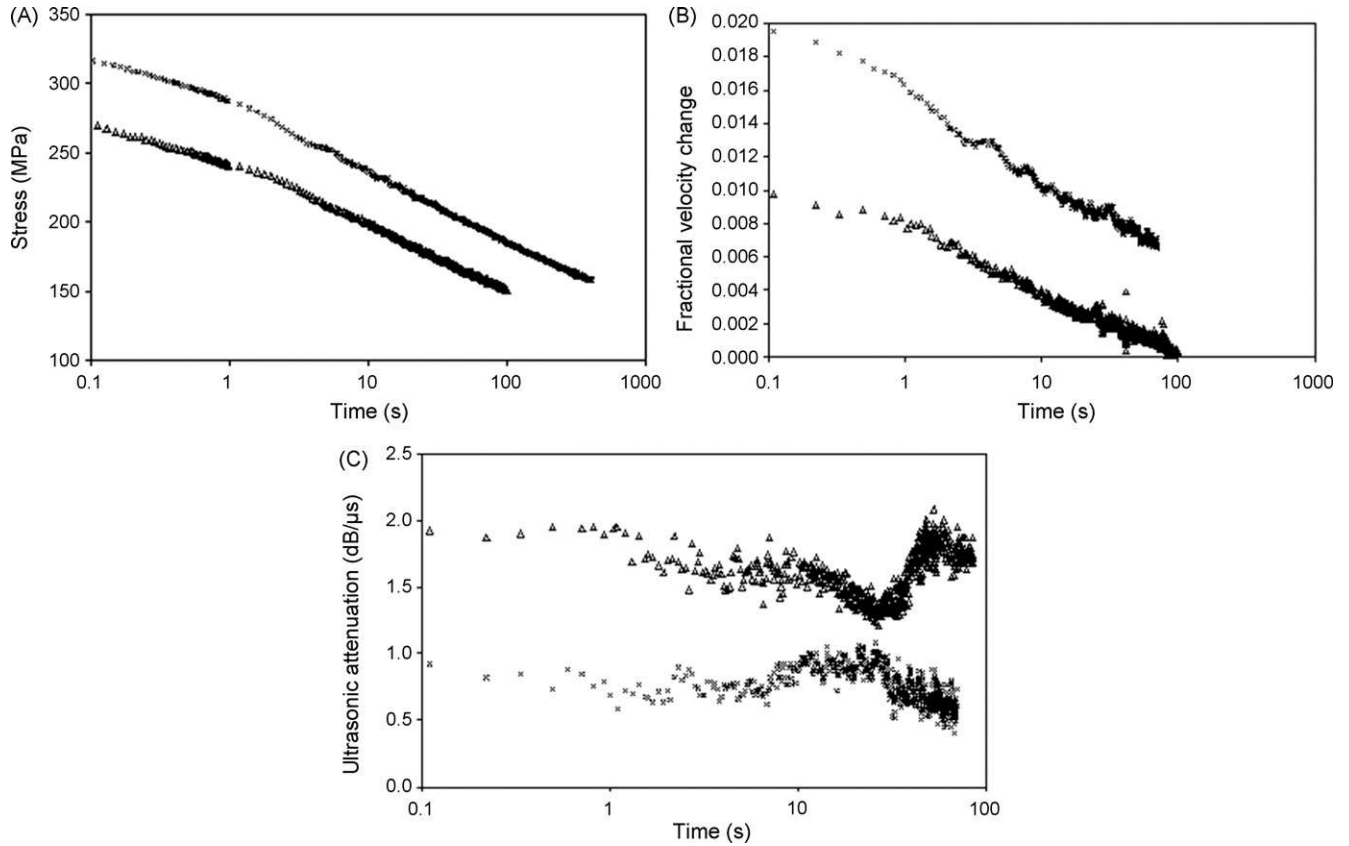
Fig. 6. (A) Stress, (B) fractional ultrasonic velocity change and (C) attenuation for $T = 550\,^{\circ}\text{C}$ and strain rate $= 0.1\,\text{s}^{-1}$. For open triangles, strain $= 0.15$. For crosses, strain $= 0.5$. Attenuation results are for an ultrasonic frequency of 8 MHz.

Hence, it is concluded that magnetomechanical damping gives only a small contribution to the experimental results.

From Fig. 6B the initial value of $\Delta v / v_0$ is much higher for the higher strain. Based on the above conclusion, this can be due to an increase in ρL^2. Other factors that control the initial values of $\Delta v / v_0$ are texture and grain scattering effects. However, the effects are difficult to estimate since firstly Eq. (14) assumes spherical grains and secondly, W_{400} in Eq. (13) can be positive or negative, thus, the velocity change can increase or decrease during deformation.

The smaller attenuation values observed in Fig. 6C for the higher strain are expected to be due to a combination of dislocation damping, i.e. smaller ρL^4 for larger strains and a difference in grain scattering compared to the lower strain case.

For the attenuation results, a constant contribution due to grain scattering effects during recovery is expected. This effect can be estimated from Eqs. (15), (18) and (19) provided that the grain size, velocities v_L and v_s, and the single crystal elastic

constants are known. The grain size was obtained from analysis of optical micrographs. For each experiment around 200 grains were analysed and the average equivalent circle diameter (ECD) obtained. For v_L, values were obtained from experimental data using the values after 100 s of annealing, whilst v_s was assumed equal to $0.5v_L$. The single crystal elastic constants were assumed equivalent to those for pure iron. In the literature Rayne and Chandrasekhar [33] have measured these constants up to room temperature. However, the experiments performed here were at higher temperatures, thus the reported temperature variation of the elastic constants was extrapolated to obtain values relevant to this study. The theoretical attenuation due to grain scattering for each of the experiments is shown in Table 2. Also shown are the calculated scattering factors and the average equivalent circle diameters.

By subtracting the theoretical attenuation due to grain scattering from each experimental result yields attenuation values that are expected to be due to dislocation damping only.

Table 2
Theoretical calculation of attenuation due to grain scattering

Temperature (°C)	Strain	S_L ($\times 10^{-10}$ s^3/m^3)	Average ECD (μm)	Calculated α_g at 8 MHz (dB/μs)
550	0.15	6.9	50	0.35
550	0.50	6.2	41	0.17
730	0.15	9.0	49	0.43
800	0.15	11.2	52	0.64

Thus, since the velocity change has been shown to mostly depend on dislocation damping, Eqs. (1)–(5) can then be used to determine the dislocation density and pinning point separation for each experiment.

Whilst the parameters G, b, C and Λ are known, the damping constant B requires further discussion.

The damping constant B is defined by the equation:

$$\tau b = B v_{dis} \tag{23}$$

where τ is the resolved shear stress that acts on the slip plane of the dislocation, b the Burgers vector, and v_{dis} is the dislocation velocity [34]. The quantity τb is the force per unit length acting on the dislocation. Thus, B can in principle be obtained from experimental measurement of dislocation velocities as a function of applied stress.

The value of B depends on a combination of damping due to (i) phonons, (ii) impurities and (iii) electrons. The effect of electrons is only significant at very low temperatures and will not be considered here. The overall B is a summation of the damping constant due to phonons B_p and the damping constant due to impurities, B_s:

(i) The damping constant due to phonons B_p in a pure metal is given by Liebfried's formula, which is quoted in the paper of Granato and Lucke [35]:

$$B_p = \frac{3kTZ}{10V_s a^2} \tag{24}$$

where k is the Boltzmann's constant, Z the number of atoms per unit cell, a the lattice parameter and V_s is the shear wave velocity in the material.

Eq. (24) has been shown to give good agreement with experimentally obtained values of B for pure metals above 50 K [34,36].

(ii) The effect of impurity drag on dislocation motion has been treated by Hirth and Lothe [37]. In the case of dragging of interstitial solute atmospheres, e.g. carbon, the damping constant B_s is given by

$$B_s = \frac{2\pi kTC_\infty}{3\omega} \tag{25}$$

where C_∞ is the concentration of the interstitial solute far from the dislocation and ω is the jump frequency of the solute in the material, given by

$$\omega = v_d \exp\left(-\frac{Q}{RT}\right) \tag{26}$$

where v_d is the Debye frequency, R the gas constant and Q is the activation energy for diffusion of the solute in the solvent [37].

Finally, Lucke and Granato [38] proposed the following relation for B_s, when the dislocations are dragging along movable point defects:
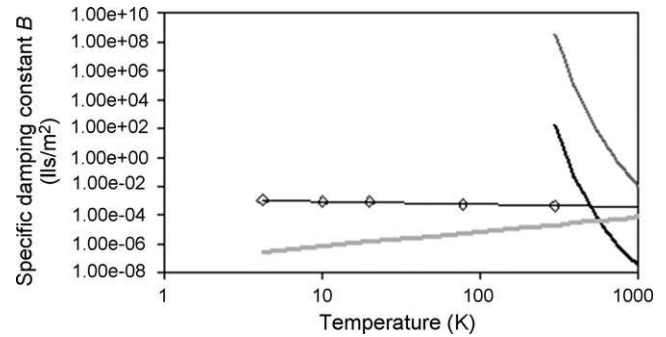
$$B_s = \frac{kT}{DL_d} \tag{27}$$

Fig. 7. Damping constant as a function of temperature: open diamonds indicate literature experimental values for iron with 1.4 ppm carbon and 0.1 ppm nitrogen [34], light grey line is Eq. (24), black line is Eq. (25) and dark grey line is Eq. (27).

where D is the diffusivity of the movable point defects and L_d is their separation along dislocations.

To decide whether to use a theoretical value for B or one from experimental data in the literature, Eqs. (24), (25) and (27) have been compared to experimentally obtained B values by Urabe and Weertman [34]. The results of the comparison are shown in Fig. 7.

As can be seen, the experimental B values in the literature decrease with increasing temperature. In addition the values are much larger than those predicted by the phonon drag mechanism (light grey line). According to the authors the damping behaviour was thought to be caused by the interaction of interstitials (C and N) with dislocations [34]. Indeed the decrease of the damping constant with increasing temperature would be consistent with a reduction in the drag due to interstitials.

The predictions of Eqs. (25) and (27) are shown by the black line and the dark grey line, respectively. In calculating B, it was assumed that the dominant solute effect was that due to carbon atoms. For Eq. (25) C_∞ was assumed to be equal to the bulk carbon concentration, whilst for Eq. (27) the separation of pinning points on dislocations (carbon atoms), was assumed to be 10 nm. This last value was chosen just to illustrate the shape of the curve obtained from Eq. (27).

As can be seen, both equations predict a decrease in damping constant with increasing temperature but they are not in quantitative agreement with the experimental values. Also, the calculated rate of decay in B is much higher than that suggested by the experimental data.

In light of the large difference between the theoretical predictions and the literature experimental data, B values for use in this study will be derived from the experimental literature data. The values of B are obtained by fitting a line to the experimental data and extrapolating it to the temperature of interest (see Fig. 7). In addition, assuming that the damping constant is proportional to the carbon concentration, the damping constant values in Fig. 8 are multiplied by the ratio of the carbon concentration in this study to that in the literature experimental study. The damping constant B to be used in the data analysis to follow can be represented by the following empirical relation:

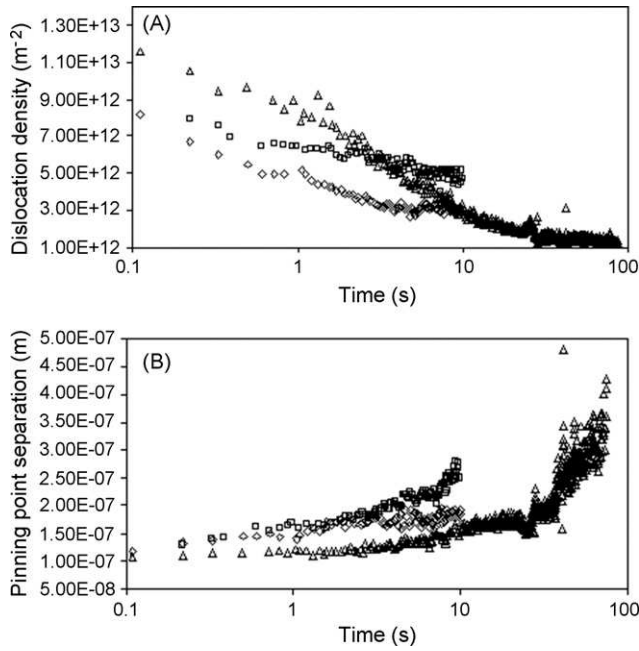$$\log B = \frac{C_0}{C_{0\,ref}}(-0.203\log(T) - 2.8003) \tag{28}$$

Fig. 8. (A) Dislocation density evolution for various temperatures. (B) Corresponding evolution in pinning point separation. Open triangles = 550 °C, open diamonds = 730 °C and open squares = 800 °C. Strain = 0.15 and strain rate = 0.1 s^{-1}.

where C_0 is the carbon concentration the steel in this study and $C_{0\,ref}$ is the concentration from the literature experimental investigation in Fig. 7 [34].

The calculated dislocation densities and pinning point separations are shown in Figs. 8 and 9. As can be seen from Fig. 8A the calculated dislocation densities decrease with time. The initial
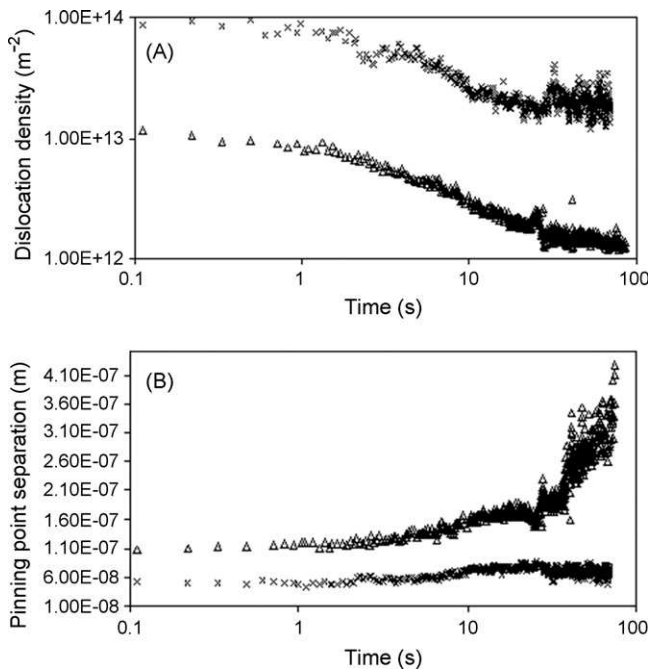

Fig. 9. (A) Dislocation density evolution for two strains. (B) Corresponding evolution in pinning point separation. Open triangles: strain = 0.15, crosses: strain = 0.5. Strain rate = 0.1 s^{-1} and T = 550 °C.

dislocation densities are expected to decrease with increasing temperature, since dynamic recovery is more rapid at higher temperatures. However, the dislocation densities at 730 °C are slightly lower than at 800 °C. Errors in the choice of v_0 and possible errors in determining the attenuation due to dislocations only, are blamed for this unexpected result.

From data in Fig. 8B it follows that the calculated pinning point separation increases with time for all temperatures. In addition, the pinning point separation is generally smaller for lower temperatures.

From Fig. 9 it follows that a higher dislocation density and a smaller pinning point separation are obtained at the higher strain. The time dependence of the dislocation density is generally similar for both strains.

The pinning point separation is expected to reflect a combination of two characteristic lengths. Firstly, the separation of carbon atoms on dislocations and secondly, the jog separation. The effect of temperature, strain and recovery on the carbon atom separation is difficult to estimate. For the jog separation, an increase in temperature should decrease the dislocation density and therefore increase the jog separation. Increasing the strain increases the dislocation density and therefore decreases the jog separation. For the recovery evolution, when the dislocation density decreases the jog separation should increase. These trends are in general agreement with the experimental results in Figs. 8B and 9B.

The evolution in dislocation density can also be calculated from the stress relaxation data using [18]:

$$\sigma_f - \sigma_y = M\alpha_1 Gb\sqrt{\rho} \tag{29}$$

where σ_f is the flow stress (assumed equal to the experimentally measured relaxation stress), σ_y the yield stress, M the Taylor factor (for BCC metals $M = 2$ [37]) and α_1 is a constant of the order 0.3 [40].

Fitting of the stress relaxation curves to a recovery model [41] allows the average activation volume over the time scale of the experiments to be determined. From this an activation length is obtained from [42]:

$$V \approx b^2 l_a \tag{30}$$

where V is the activation volume and l_a is the activation length. This length is expected to be equal to the jog separation or the carbon atom separation on dislocations, depending which obstacle is controlling the rate of dislocation glide [40].

A comparison of the dislocation densities and pinning point separations, obtained from the stress and ultrasonic parameters, is shown in Figs. 10 and 11 for two strain levels.

From Figs. 10A and 11A it can be seen that the dislocation densities calculated from the ultrasonics data are considerably lower than those calculated from the stress. For the lower strain the difference is two orders of magnitude whilst for the higher strain it is one order of magnitude. For the pinning point separation the values obtained from the stress are about one order of magnitude smaller than those obtained from the ultrasonics. The difference is the same for both low and high strains at 550 °C.
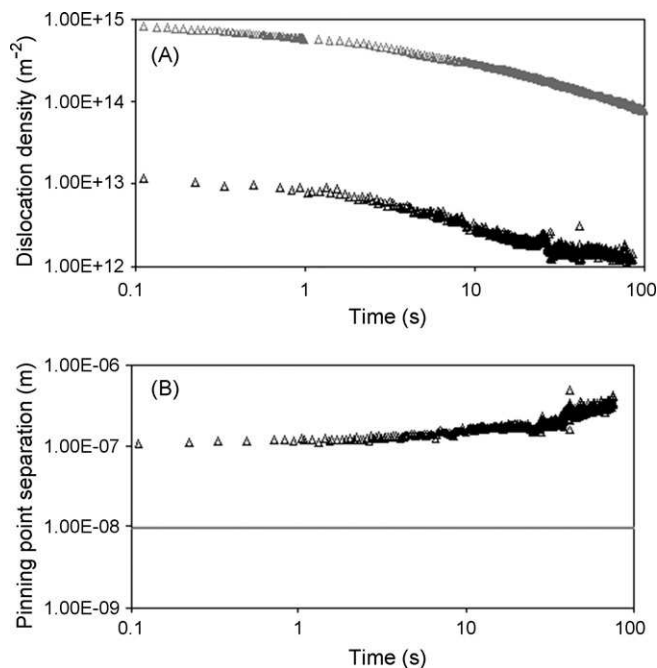
Fig. 10. (A) Dislocation density evolution. Open black triangles represent ultrasonic values, open dark grey triangles represent stress relaxation values. (B) Dislocation loop length. Open black triangles represent ultrasonic values, dark grey line is average loop length from stress relaxation values. For both figures: $T = 550\,^{\circ}\text{C}$, strain = 0.15 and strain rate = $0.1\,\text{s}^{-1}$.

For the calculated dislocation densities the difference can be explained with reference to the dislocation structure. Eq. (29) involves a total dislocation density, including contributions from both mobile dislocations, e.g. in cell interiors, and immobile dislocations, e.g. in cell walls. The dislocations that cause damping of the ultrasonic waves, however, are free to vibrate in response to the ultrasonic stress [11]. Thus, the dislocation density "detected" by the ultrasonics method is likely to be dominated by mobile dislocations in the cell interior, rather than by relatively immobile dislocations in the cell walls. Since the dislocation density in cell walls is generally higher than in cell interiors, the values calculated from the ultrasonics data should be lower.

The difference in the values of the pinning point separation is understandable, since the pinning point separation for the stress is defined differently to that determining the ultrasonics, as explained earlier.

Part of the differences in calculated dislocation densities and pinning point separations could be due to the values of the damping constant B. The values have been estimated from experimental values determined for iron in the literature with 17 times less carbon. Although this was taken into account by assuming that B is proportional to the concentration of carbon, there still could be some uncertainty in this assumption. In addition, if B was used as a fitting parameter, a single value of B could not give good agreement for all the data in Figs. 10 and 11. Thus, this strengthens the view that the dislocations "detected" by ultrasonics are not the same as those "detected" by the stress relaxation technique.
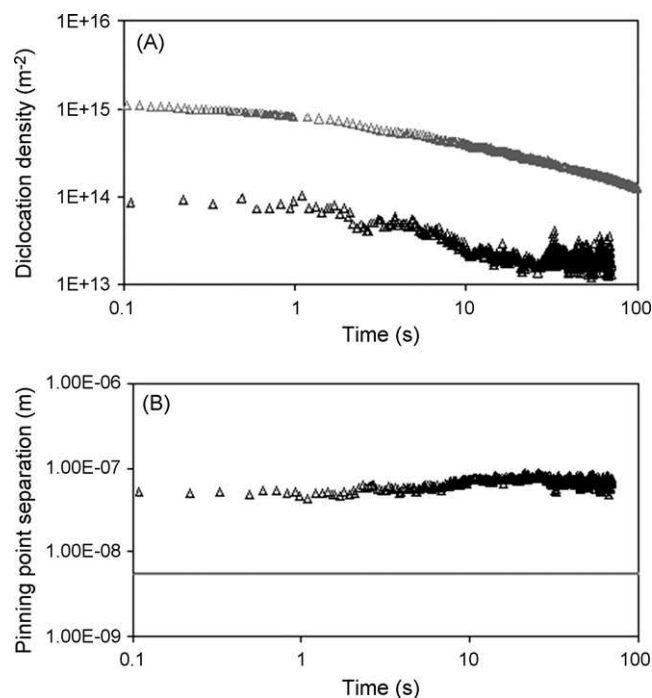

Fig. 11. (A) Dislocation density evolution. Open black triangles represent ultrasonic values, open dark grey triangles represent stress relaxation values. (B) Dislocation loop length. Open black triangles represent ultrasonic values, dark grey line is average loop length from stress relaxation values. For both figures: $T = 550\,^{\circ}\text{C}$, strain = 0.5 and strain rate = $0.1\,\text{s}^{-1}$.
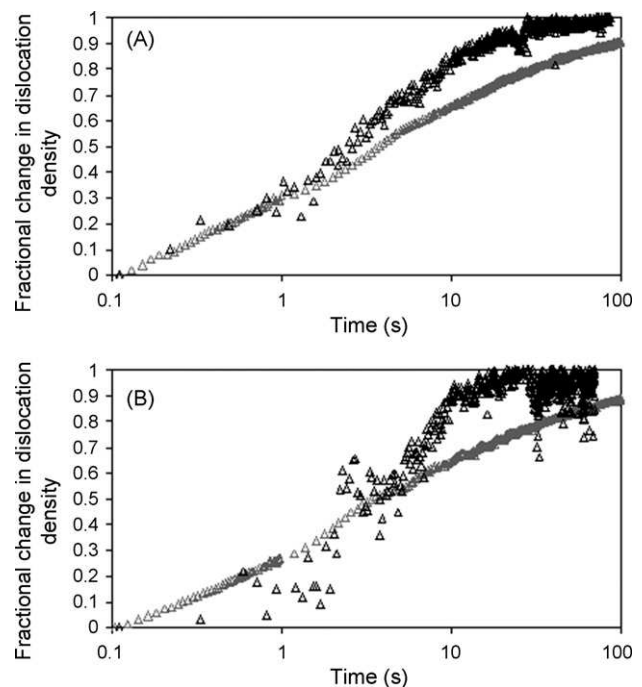

Fig. 12. Change in dislocation density calculated from ultrasonics data (open black triangles) and for stress relaxation data (open grey triangles): (A) $T = 550\,^{\circ}\text{C}$, strain = 0.15, strain rate = $0.1\,\text{s}^{-1}$ and (B) $T = 550\,^{\circ}\text{C}$, strain = 0.5, strain rate = $0.1\,\text{s}^{-1}$.

Finally, the fractional change F in dislocation density can be calculated and compared for both sets of data in Figs. 10A and 11A using:

$$F = \frac{\rho_i - \rho(t)}{\rho_i - \rho_f} \tag{31}$$

where ρ_i is the initial dislocation density, $\rho(t)$ the value at time t after deformation and ρ_f is the final or minimum value calculated.

Fig. 12A and B shows the fractional change in dislocation density obtained from the data in Figs. 10A and 11B.

As can be seen for both strains, the rate of change in dislocation density appears to be more rapid for the ultrasonics compared with the values calculated from the stress.

Since the rate of change in dislocation density is independent of the damping constant B, the difference is most likely due to the fact that the ultrasonic waves are more sensitive to dislocations in the cell interior, which might be expected to have different annihilation rates compared to those in cell walls.

6. Conclusions

(1) For the first time, laser ultrasonics has been applied to the study of recovery in ferrite following warm deformation. In addition the stress relaxation method was used simultaneously with laser ultrasonics. This allowed a comparison to be made concerning the sensitivity of the two techniques to the recovery process.
(2) The recovery process was revealed by the change in stress, ultrasonic velocity and attenuation.
(3) Application of the vibrating string model for dislocation damping [26] allowed the determination of the dislocation density and pinning point separation during recovery.
(4) This was compared to the corresponding values calculated from the stress relaxation technique. The results showed a difference of between two orders and one order of magnitude for dislocation density. The pinning point separations differed by one order of magnitude.
(5) The observed differences in dislocation densities were thought to be due the stress reflecting all dislocations, while the ultrasonic waves were thought to be more sensitive to mobile dislocations in cell interiors.
(6) The rate of change in dislocation density was higher for the ultrasonic values compared to the stress. This strengthens the view that the dislocations detected by ultrasonics are mobile dislocations in cell interiors.

References

[1] S. Sundin, D. Artymowicz, Metall. Mater. Trans. A 33 (2002) 687–691.
[2] M. Dubois, M. Militzer, A. Moreau, J. Bussiere, Scr. Mater. 42 (2000) 867–874.
[3] E. Ulmgren, M. Ericsson, D. Artymowicz, B. Hutchinson, Mater. Sci. Forum 467–470 (2004) 1353–1362.
[4] M. Dubois, A. Moreau, M. Militzer, J. Bussiere, Scr. Mater. 39 (6) (1998) 735–741.
[5] S.E. Kruger, E.B. Damm, Mater. Sci. Eng. A 425 (2006) 238–243.
[6] S.E. Kruger, A. Moreau, M. Militzer, T. Biggs, Mater. Sci. Forum 426–432 (2003) 483–488.
[7] S.E. Kruger, G. Lamouche, A. Moreau, M. Militzer, Materials Science and Technology Conference Proceedings, 2004, pp. 809–812.
[8] G. Lamouche, S.E. Kruger, L. Gille, N. Giguère, S. Bolognini, A. Moreau, in: D.O. Thompson, D.E. Chimenti (Eds.), Review of Progress in Quantitative NDE, vol. 22, AIP, New York, 2003, pp. 1681–1688.
[9] A. Moreau, M. Lord, D. Levesque, M. Dubois, J. Bussiere, J. Alloys Compd. 310 (2000) 427–431.
[10] S. Bolognini, A. Moreau, J. Appl. Phys. 94 (6) (2003) 3771–3780.
[11] T. Ohtani, H. Ogi, M. Hirao, Metall. Mater. Trans. A 36 (2005) 411–420.
[12] H. Ogi, H. Ledbetter, S. Kim, Metall. Mater. Trans. A 32 (2001) 1671–1677.
[13] M. Hirao, H. Ogi, N. Suzuki, T. Ohtani, Acta Mater. 48 (2000) 517–524.
[14] S. Kenderian, et al., Mater. Sci. Eng. A 348 (2003) 90–99.
[15] B. Hutchinson, et al., Ironmak. Steelmak. 29 (1) (2002) 77–80.
[16] A. Moreau, et al., Ultrasonics 40 (2002) 1047–1056.
[17] G. Jeskey, R. Kolarik II, E. Damm, J. Monchalin, G. Lamouche, S. Kruger, M. Choquet, Materials Science and Technology Conference Proceedings, 2004, pp. 823–830.
[18] A. Smith, H. Luo, D.N. Hanlon, J. Sietsma, S. van der Zwaag, ISIJ Int. 44 (7) (2004) 1188–1194.
[19] L.P. Karjalainen, Mater. Sci. Technol. 11 (1995) 557–565.
[20] L.P. Karjalainen, J. Perttula, ISIJ Int. 36 (6) (1996) 729–736.
[21] H. Luo, J. Sietsma, S. van der Zwaag, Metall. Mater. Trans. A 35 (6) (2004) 1889–1898.
[22] M. Barnett, J. Jonas, ISIJ Int. 37 (7) (1997) 697–705.
[23] M. Barnett, J. Jonas, ISIJ Int. 37 (7) (1997) 706–714.
[24] D. Liu, A. Humphreys, M. Toroghinezhad, J. Jonas, ISIJ Int. 42 (7) (2002) 751–759.
[25] B. Basu, M. Mehta, S. Pattalwar, J. Magn. Magn. Mater. 23 (1981) 241–246.
[26] A. Granato, K. Lucke, J. Appl. Phys. 27 (6) (1956) 583–593.
[27] A. Nowick, B. Berry, Anelastic Relaxation in Crystalline Solids, Academic Press, New York, 1972.
[28] J. Degauque, Mater. Sci. Forum 366–368 (2001) 453–482.
[29] V. Coronel, D. Beshers, J. Appl. Phys. 64 (4) (1988) 2006–2015.
[30] W. Mason, Phys. Rev. 83 (1951) 683–684.
[31] S. Hirsekorn, J. Acoust. Soc. Am. 72 (1982) 1021–1031.
[32] E. Papadakis, E. Reed, J. Appl. Phys. 32 (4) (1961) 682–687.
[33] J.A. Rayne, B.S. Chandrasekhar, Phys. Rev. 122 (1961) 1714–1716.
[34] N. Urabe, J. Weertman, Mater. Sci. Eng. 18 (1975) 41–49.
[35] A. Granato, K. Lucke, J. Appl. Phys. 27 (7) (1956) 789–805.
[36] V. Parameswaran, N. Urabe, J. Weertman, J. Appl. Phys. 43 (7) (1972) 2982–2986.
[37] J. Hirth, J. Lothe, Theory of Dislocations, 2nd ed., Krieger Publishing Company, Malabar, FL, 1982.
[38] K. Lucke, A. Granato, Phys. Rev. B 24 (12) (1981) 6991–7006.
[40] E. Nes, Acta Mater. 43 (1995) 2189–2207.
[41] M. Verdier, Y. Brechet, P. Guyot, Acta Mater. 47 (1999) 127–134.
[42] E. Nes, Prog. Mater. Sci. 41 (1998) 129–193.